Inorganic Chemistry

Article

pubs.acs.org/IC

Ferromagnetic Order, Strong Magnetocrystalline Anisotropy, and Magnetocaloric Effect in the Layered Telluride $Fe_{3-\delta}GeTe_2$

Valeriy Yu. Verchenko,[†,‡] Alexander A. Tsirlin,[‡,§] Alexei V. Sobolev,[†] Igor A. Presniakov,[†] and Andrei V. Shevelkov*[,†]

[†]Department of Chemistry, Lomonosov Moscow State University, 119991 Moscow, Russia

[‡]National Institute of Chemical Physics and Biophysics, 12618 Tallinn, Estonia

[§]Experimental Physics VI, Center for Electronic Correlations and Magnetism, Institute of Physics, University of Augsburg, 86135 Augsburg, Germany

Supporting Information

ABSTRACT: The ternary transition-metal compound $Fe_{3-\delta}GeTe_2$ is formed for $0 < \delta < 0.3$. X-ray diffraction and Mössbauer spectroscopy reveal its layered crystal structure with occasional Fe vacancies in the Fe2 site, whereas no Fe atoms occupy the interlayer space, so that only van der Waals interactions exist between adjacent layers. We explore magnetic behavior and ensuing functional properties of $Fe_{2.9}GeTe_2$ via neutron diffraction, thermodynamic and transport measurements, Mössbauer spectroscopy, and electronic structure calculations. Below $T_C = 225$ K, $Fe_{2.9}GeTe_2$ is ferromagnetically ordered with the magnetic moments of 1.95(5) and 1.56(4) μ_B at $T = 1.5$ K, both directed along *c*, which is the magnetic easy axis. Electronic structure calculations confirm this magnetic structure and reveal a remarkably high easy-axis anisotropy of 4.2 meV/f.u. Mössbauer spectra reveal the magnetic ordering too, although a drastic influence of Fe vacancies on quadrupolar splittings and local magnetic fields has been observed. A moderate magnetocaloric effect with the magnetic entropy change upon the ferromagnetic ordering transition, $-\Delta S \sim 1.1$ J·kg^{-1}·K^{-1} at 5 T, is found.

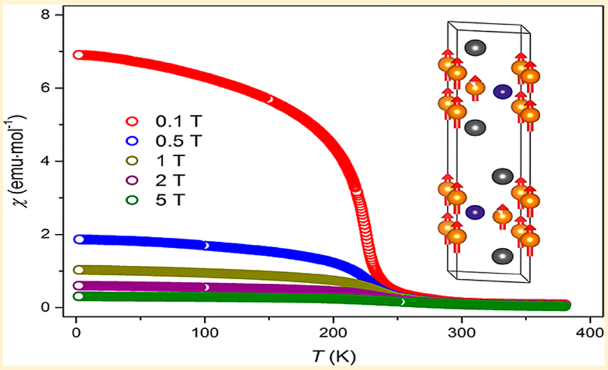

■ INTRODUCTION

The chemical bonding and electronic structure of intermetallic compounds remain an important issue in inorganic chemistry. For many classes of intermetallics, only empirical rules have been developed that help in understanding relations between the composition and crystal and electronic structure of compounds and their properties. Some of these rules have been known for years, such as the Hume-Rothery rule,[1] the others developed in the last decades, including the 14 $\bar{e}$ rule for chimney-ladder phases.[2] Only recently, such empirical rules started receiving explanations, for which the knowledge of the experimental electronic structure is of great significance.[3] In particular, this is true for numerous compounds formed by a combination of a transition metal and a *p*-block metal or semimetal. In such compounds, a strong hybridization between *d* and *p* states gives rise to unexpected features of the electronic structure and, hence, peculiarities in transport and magnetic properties.[4]

A very interesting class of metal-rich compounds with an intricate electronic structure is represented by Ni-based layered tellurides, which feature peculiarities in the crystal structure and physical properties. Various isostructural representatives with the general formula $Ni_{3\pm\delta}E_{1-y}Te_{2+y}$ (E: *p* element of groups 13−15) are known, such as $Ni_{3-\delta}GaTe_2$,[5] Ni_3GeTe_2,[6] $Ni_{3\pm\delta}In_{1-y}Te_{2+y}$,[7] $Ni_{3-\delta}SnTe_2$,[8] and Ni_2SbTe_2.[9] Each of them possesses the crystal structure that could be regarded as a derivative of the NiAs motif. In this derivative, $[Ni_3E]$ heterometallic slabs are confined by Te atoms in separate layers, which alternate along the *c* direction of a hexagonal unit cell. Thereby, crystal structures consist of alternating layers containing metallic blocks of *d* and *p* elements. Both the *d*−*p* bonding and layered character of the crystal structure may lead to peculiarities in physical properties, which call for a detailed study. However, Ni-based layered tellurides are metals and Pauli paramagnets.[5,6,9] By analyzing electronic structures of these compounds, one finds that Ni behaves as an effectively d^{10} center, which explains the nonmagnetic character of most of the Ni derivatives.[5,10] Similar compounds with fewer valence electrons are expected to have more peculiar magnetic properties. However, Co-based analogues, surprisingly, do not exist, and only one Fe-based representative is known so far, namely, Fe_3GeTe_2 that is indeed significantly different from Ni-based layered tellurides.[6] Fe_3GeTe_2 is reportedly metallic and

Received: June 3, 2015
Published: August 12, 2015

DOI: 10.1021/acs.inorgchem.5b01260

ferromagnetic below $T_C \sim 230$ K; however, a closer look at the magnetization data reveals nontypical behavior: the magnetization continues increasing in higher magnetic fields, and even at 7 T, the saturation of the magnetic moment is not reached.[6] This observation may indicate a more complex nature of the magnetic order, such as canted antiferromagnetic or ferrimagnetic.

In this paper, we report on a comprehensive study of chemical, thermodynamic, and transport properties of $Fe_{3-\delta}GeTe_2$ and employ a neutron diffraction technique and ^{57}Fe Mössbauer spectroscopy to investigate its magnetism and electronic structure in detail. We demonstrate how the magnetism of $Fe_{3-\delta}GeTe_2$ reflects its functional properties, such as magnetocaloric effect. We also show that the combination of itinerant ferromagnetic behavior with the layered character of the crystal structure gives rise to a strong magnetocrystalline anisotropy, energy of which was carefully extracted within full relativistic band structure calculations.

■ EXPERIMENTAL SECTION

Synthesis. The synthesis of $Fe_{3-\delta}GeTe_2$ powder was performed by the standard ampule technique. The elements, Fe (powder, Acros, 99%), Ge (chips, Sigma Aldrich, 99.999%), and Te (pieces, Sigma Aldrich, 99.999%), were used as starting materials. To examine the homogeneity range of $Fe_{3-\delta}GeTe_2$, we synthesized specimens with $0 \leq \delta \leq 0.3$. The mixtures of starting materials were placed in quartz ampules, which were then sealed under a vacuum of 2×10^{-2} Torr. Ampules were annealed at 625 °C during 5 days, and furnace cooled to room temperature. After the first annealing, the specimens were ground in an argon glovebox (MBRAUN 120B-G, $p(H_2O, O_2) < 1$ ppm), sealed in quartz ampules, annealed at 625 °C for 5 more days, and furnace cooled again. Finally, the samples were ground in an argon glovebox and stored under a pure argon atmosphere before any operations.

Characterization. Phase composition and crystal structure were investigated by the standard X-ray technique using a BRUKER D8 Advance diffractometer (Cu Kα_1 radiation, Ge monochromator, $\lambda = 1.540598$ Å). For the phase composition analysis, the program package STOE WinXPOW was used. The crystal structure refinement was performed using the Rietveld method in JANA 2006 software.[11] In all cases, the crystal structure data of Fe_3GeTe_2 obtained earlier by Deiseroth et al. were used as a starting model including the possible presence of the Fe3 (0; 0; 0.5) site in the crystal structure, as found in the Ni analogue.[6] Details of the data collection and refinement are shown in Table 1. Atomic parameters and selected interatomic distances are listed in Tables 2 and 3, respectively.

Table 1. Crystal Data Collection and Refinement Parameters for $Fe_{2.9}GeTe_2$ at 300 K from XRD Data

parameter	value
refined composition	$Fe_{2.888(4)}GeTe_2$
composition from EDXS	$Fe_{2.89(6)}Ge_{0.96(5)}Te_{2.00(8)}$
space group	$P6_3/mmc$ (No. 194)
a [Å]	4.00848(2)
c [Å]	16.3307(1)
V [Å^3]	227.246(2)
Z	2
ρ_{calc} [g·cm^{-3}]	7.15
μ [mm^{-1}]	179.15
2θ range [deg]	9−100
R_p ($\times 10^{-2}$)	3.7
R_{wp} ($\times 10^{-2}$)	5.2
GOF	1.59

Table 2. Atomic Parameters for $Fe_{2.9}GeTe_2$

atom	site	x	y	z	occupancy	U_{iso} [Å^2]
Fe1	4e	0	0	0.6704(1)	1	0.0333(4)
Fe2	2c	2/3	1/3	3/4	0.888(4)	0.0219(8)
Ge1	2d	1/3	2/3	3/4	1	0.0139(4)
Te1	4f	2/3	1/3	0.58999(5)	1	0.0125(2)

Table 3. Selected Interatomic Distances for $Fe_{2.9}GeTe_2$[a]

bond		distance [Å]
Ge1	−Fe1 (×6)	2.655
	−Fe2 (×3)	2.314
Fe1	−Fe1 (×1)	2.602
	−Fe2 (×3)	2.655
	−Ge1 (×3)	2.655
	−Te1 (×3)	2.661
Fe2	−Ge1 (×3)	2.314
	−Te1 (×2)	2.613
	−Fe1 (×6)	2.655

[a] Note: SDs are all equal to or less than 0.001 Å

Elemental composition was studied by energy-dispersive X-ray spectroscopy (EDXS) employing a JSM JEOL 6490LV scanning electron microscope operated at 30 kV and equipped with an EDX detection system INCA x-Sight. The specimens were pressed at room temperature and 80−100 bar pressure in cylindrical pellets, which were then fixed on a sample holder. Distribution of the elements across the surface was investigated by mapping, and elemental composition of each specimen was determined by averaging the data of 10 point acquisition spectra. In all cases, the EDX detection system was calibrated by using elemental Co as a standard.

Electronic and Magnetic Structure Calculations. The crystal structure parameters of $Fe_{2.9}GeTe_2$ obtained from the Rietveld refinement of powder XRD data were used in electronic and magnetic structure calculations assuming fully occupied Fe1 and Fe2 sites. The calculations were performed within the density functional theory (DFT) approach as implemented in the FPLO code (version 9.05-39).[12] Local density approximation (LDA) was used to treat the exchange-correlation energy.[13] The k-space integration was performed by an improved tetrahedron method[14] on a grid of $48 \times 48 \times 48$ k and $24 \times 24 \times 24$ points for spin-unpolarized and spin-polarized calculations, respectively. In the scalar relativistic spin-polarized calculations, we used ferro-, antiferro-, and ferrimagnetic initial spin splits, but all calculations converged to the ferromagnetic ground state. Therefore, the magnetocrystalline anisotropy (MCA) energy of Fe_3GeTe_2 was calculated for the ferromagnetic spin configuration. Having achieved the required energy convergence on the grid of $24 \times 24 \times 24$ k points, we calculated the MCA energy including spin−orbit coupling (SO) only or spin−orbit coupling with the orbital polarization correction (SO+OP).[15] Fe 3d orbitals located on the Fe1 and Fe2 sites were used for the correction.

Thermodynamic and Transport Properties Measurements. Magnetization of the $Fe_{2.9}GeTe_2$ pellet (prepared in the same way as for EDXS) was measured with the VSM setup of the Physical Property Measurement System (PPMS, Quantum Design) in external magnetic fields between 0 and 14 T in the temperature range from 2 to 380 K.

Heat capacity measurements were performed with a relaxation-type calorimeter (PPMS, Quantum Design) in zero magnetic field between 1.9 and 50 K.

Thermoelectric properties were measured using the four-probe method with the TTO setup of PPMS (Quantum Design) in the temperature range of 4−400 K in zero magnetic field. Thermal and electrical contacts (gold-plated Pb stripes) were fixed on a rectangular-shaped pellet with a size of $8 \times 3 \times 1$ mm^3 using silver-containing epoxy resin (Epotek H20E) hardened at 100 °C. The pellet was cold pressed from the powder at an external pressure of 100 bar. Density of the obtained pellet was estimated from its linear dimensions and mass to be 85% of the theoretical value.

Magnetic Structure Investigation. Neutron powder diffraction (NPD) data for the magnetic structure refinement were collected with the DMC powder diffractometer at the Swiss spallation neutron source (SINQ, Paul Scherrer Institute (PSI), Villigen, Switzerland). The data were collected with the wavelength λ = 2.46 Å at temperatures between 1.5 and 300 K using a standard orange cryostat. Rietveld refinements against the NPD data were performed with the JANA 2006 package.[11]

Mössbauer Spectroscopy. ^{57}Fe Mössbauer spectra were recorded at 77 and 300 K using a conventional constant-acceleration spectrometer MS-1104Em in the transmission geometry. A radiation source ^{57}Co(Rh) was kept at room temperature. All isomer shifts are referred to α-Fe at 300 K. Experimental spectra were processed and analyzed using methods of spectral simulations implemented in the SpectrRelax program.[16]

■ RESULTS AND DISCUSSION

Synthesis and Homogeneity Range. $Fe_{3-\delta}GeTe_2$ could be easily prepared by the direct reaction of elements in an evacuated quartz ampule. Annealing of elements yields black powders of the reaction product on the bottom of quartz ampules. No condensation of side products was observed in other parts of the ampules. Thus, the standard ampule technique is a facile way to obtain $Fe_{3-\delta}GeTe_2$ with the well defined nominal composition.

Nonstoichiometry and vacancies are often observed in Ni-based mixed tellurides with the general formula $Ni_{3\pm\delta}E_{1-y}Te_{2+y}$ (E = Ga, In, Ge).[5−7] For instance, $Ni_{3-\delta}GaTe_2$ adopts a wide homogeneity range $0 \leq \delta \leq 0.65$, which is caused by the partial occupation of different crystallographic sites by Ni atoms. In the case of $Ni_{3+\delta}In_{1-y}Te_{2+y}$, the values of δ and y can reach 0.32 and 0.14, respectively, even causing a superstructure formation. To examine the homogeneity range and determine phase boundaries of $Fe_{3-\delta}GeTe_2$, we investigated the phase and elemental composition of specimens with different values of δ by using the standard X-ray diffraction technique and EDX spectroscopy. The results are presented in Figure 1. Indeed, $Fe_{3-\delta}GeTe_2$ displays nonstoichiometry like isostructural layered tellurides. The specimen with $\delta = 0$ reproducibly contained ~2 wt. % of $Fe_{1+\delta}Te$ ($P4/nmm$, Cu_2Sb type). This admixture was also detected by EDXS. By increasing δ, we were able to prepare single phase specimens up to $\delta = 0.3$ where $FeTe_2$ ($Pnnm$, FeS_2 type) appeared as an impurity phase. In summary, the homogeneity range of $Fe_{3-\delta}GeTe_2$ is $0 < \delta < 0.3$, where lattice parameters decrease monotonically with increasing δ. A single phase specimen with the composition $Fe_{2.9}GeTe_2$ (δ = 0.1) was used in all subsequent measurements.

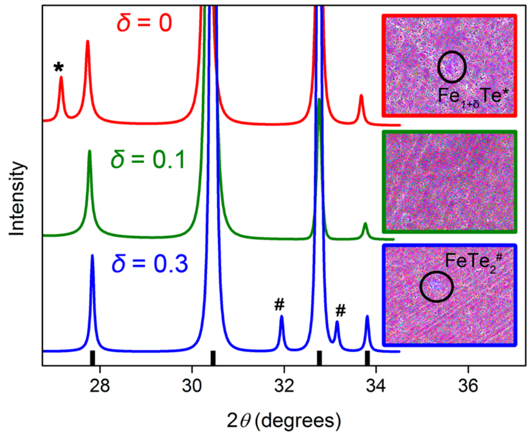

Figure 1. XRD patterns and EDXS composition maps of $Fe_{3-\delta}GeTe_2$. On the composition maps, Fe is presented in red color, Ge in green, and Te in blue.

Crystal Structure Refinement. The crystal structure of $Fe_{2.9}GeTe_2$ was investigated by the Rietveld refinement from X-ray powder diffraction data (Figure 2). The powder XRD pattern of $Fe_{2.9}GeTe_2$ was fitted in the $P6_3/mmc$ (No. 194) space group with the lattice parameters a = 4.00848(2) Å and c = 16.3307(1) Å using atomic parameters of Fe_3GeTe_2 reported earlier in the literature as a starting model.[6] While $Fe_{2.9}GeTe_2$ is generally isostructural to Ni-based layered tellurides,[5−7] the distribution of iron atoms deserves a detailed discussion. Our refinement yields the partially occupied Fe2 site and zero occupancy for the Fe3 site, leading to the $Fe_{2.888(4)}GeTe_2$ overall composition (Tables 1 and 2) in good agreement with the nominal one and with that obtained by EDXS. Attempts to add artificially the interlayer Fe3 site with the fixed 10% occupation resulted in a considerable increase of the profile R-factors, whereas a subsequent refinement of the Fe3 site occupation gave zero within the standard deviation. The absence of the Fe3 atom is the most important difference between $Fe_{2.9}GeTe_2$ and its Ni-based analogues. Unlike the latter, $Fe_{2.9}GeTe_2$ possesses the layered crystal structure, which contains no Fe atoms in the interlayer region, and only van der Waals interactions exist between the adjacent layers.

Crystal Structure Description. A general view of the crystal structure of $Fe_{2.9}GeTe_2$ is given in Figure 3. The unit cell contains two [$Fe_{2.9}GeTe_2$] layers alternating along the c direction. In the middle of each layer, there is a 6^3 net formed by the Ge1 and Fe2 atoms. The distance between Ge1 and Fe2 in $Fe_{2.9}GeTe_2$ is 2.31 Å (Table 3), which is noticeably shorter than typical Fe−Ge distances in FeGe[17a] ($P6/mmm$, CoSn type), 2.50 Å, and $FeGe_2$[17b] ($I/4mcm$, $CuAl_2$ type), 2.56 Å, indicating strong Fe2−Ge1 interactions within the [$Fe_{2.9}GeTe_2$] layers.

The structure of the [$Fe_{2.9}GeTe_2$] layers (Figure 3b) can be described as follows. The Fe1 atoms are octahedrally coordinated by three Ge1 atoms and three Te1 atoms. The $(Ge1)_3$ edges of the octahedra are condensed on the 6^3 net in the middle of the [$Fe_{2.9}GeTe_2$] layer. Thus, each layer is composed by two slabs of edge-shared $Fe1(Ge1)_3(Te1)_3$ octahedra with the $(Ge1)_3$ edges consolidated in the middle of the layer and $(Te1)_3$ edges forming a plain net, which confines the layer. The [$Fe_{2.9}GeTe_2$] layers are separated by Te atoms, and a van der Waals gap exists between them in $Fe_{2.9}GeTe_2$, since no Fe atoms occupy the Fe3 interstitial site.

Electronic and Magnetic Structure Calculations. Using the crystal data obtained from the Rietveld refinement of powder XRD data, we calculated the electronic structure of Fe_3GeTe_2 assuming fully occupied Fe1 and Fe2 sites. Spin-unpolarized calculations yield metallic behavior with a high electronic density of states (DOS) at the Fermi level, 13.6 states/(eV·f.u.), suggesting that the Stoner mechanism of itinerant ferromagnetism may be operative. Indeed, spin-polarized calculations converged to the ferromagnetic ground state with the substantially reduced DOS at the Fermi level [3.9 states/(eV·f.u.)] and the magnetic moments of 2.5 and 1.5 μ_B on the Fe1 and Fe2 sites, respectively. The DOS at the Fermi level yields the Sommerfeld coefficient $\gamma_{bare} = 9.2$ mJ·mol^{-1}·K^{-2}.

Total and partial DOS are shown in the top panel of Figure 4. All atoms significantly contribute to the total DOS, forming

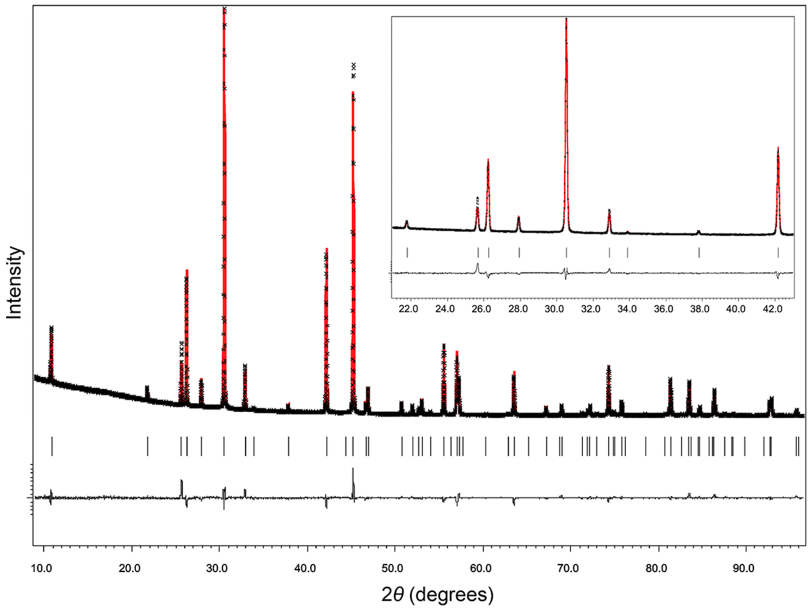

Figure 2. Experimental (black points) and calculated (red line) powder XRD patterns of $Fe_{2.9}GeTe_2$. Peak positions are given by black ticks; the difference plot is shown as a black line in the bottom part.

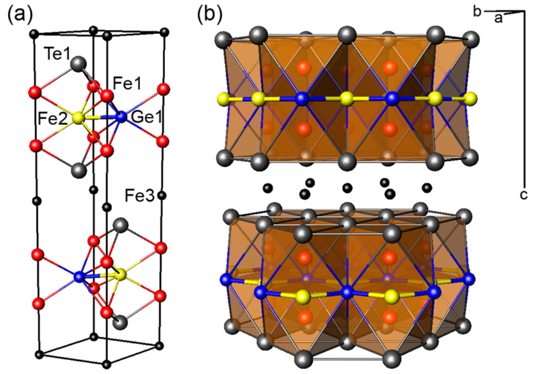

Figure 3. View of $Fe_{2.9}GeTe_2$ crystal structure: (a) unit cell and (b) polyhedral representation. The Fe3 position is vacant and shown only for comparison.

sharp peaks in both spin channels. These peaks indicate a relatively strong bonding between the Fe1 and Fe2 *d* orbitals and the Ge1 and Te1 valence orbitals. The states below −2 eV have predominantly bonding character, for which the reduction in the difference between spin channels with lowering relative energy is observed. For the energy region above −2 eV, the sharp spectral peaks formed by the Fe1 and Fe2 atoms are present. This region could be assigned to nonbonding and antibonding states. The states at the Fermi level arise mainly from the Fe1, Fe2, and Te1 contributions. Remarkably, the Fermi level is located near the DOS minimum for the spin-down channel and crosses the smooth peak in the spin-up channel, indicating a ferromagnetic and metallic ground state. From the metallic nature of Fe_3GeTe_2 and the relatively low magnetic moments on Fe, we infer that the ferromagnetic ordering in Fe_3GeTe_2 has itinerant origin.

In-plane and out-of-plane orientations of the magnetic moment turn out to result in different total energies of the system. Using fully relativistic band-structure calculations, where spin−orbit (SO) coupling is taken into account, we estimated that the ferromagnetic configuration with spins directed along the *c* axis is by 4.2(3.4) meV/f.u. more stable than the configuration with spins in the *ab* plane. Here, the number in brackets refers to the SO+OP calculation, where effects of the orbital polarization (OP) are additionally included. This magnetocrystalline anisotropy of about 6.0×10^6 (4.8×10^6) $J \cdot m^{-3}$ is quite large for an itinerant magnet and can be compared with, e.g., 30×10^6 $J \cdot m^{-3}$ in $SmCo_5$, one of the most anisotropic itinerant magnets.

To reveal the origin of this strong magnetocrystalline anisotropy, we calculated orbital moments on Fe (Table 4). The orbital moment on Fe1 is larger than the moment on Fe2 and correlates with the analysis of atomic-resolved DOS. In Figure 4, we show atomic contributions to the difference DOS for the [001] and [100] directions of the magnetization. The difference is clearly rooted in the Fe1 states. Compared to Fe2, the local environment of Fe1 is somewhat more asymmetric indeed, because Fe1 sites are on the rim of the $[Fe_3GeTe_2]$ slab. However, it may be difficult to establish a simple relation between the structural features and magnetocrystalline anisotropy given the itinerant nature of the system that implies strong electron delocalization and the loss of atomic character of individual *d* electrons.

Magnetic Properties. To challenge our computational results, we studied the magnetic structure experimentally and started with the magnetic susceptibility of $Fe_{2.9}GeTe_2$ in different applied magnetic fields. Figure 5a shows that the magnetic susceptibility increases rapidly at temperatures below 240 K, indicating the ferromagnetic transition. The transition temperature could be carefully extracted from the Fisher's heat capacity ($\partial(\chi T)/\partial T$) plot, which passes through the minimum located at $T = T_C$. Figure 5b shows that the Curie temperature of $Fe_{2.9}GeTe_2$ is $T_C \sim 225$ K. However, the behavior of $Fe_{2.9}GeTe_2$ is not reminiscent of ordinary ferromagnets, since the magnetization curve taken at $T = 2$ K (inset in Figure 5a) saturates very slowly, and even at high fields near 14 T $M(H)$ behaves linearly, giving the saturation moment $M_S = 1.0$ μ_B per Fe atom. The obtained value of M_S is significantly lower than the value extracted from the single crystal magnetization data, for which $M_S = 1.625$ μ_B when a magnetic field is applied along

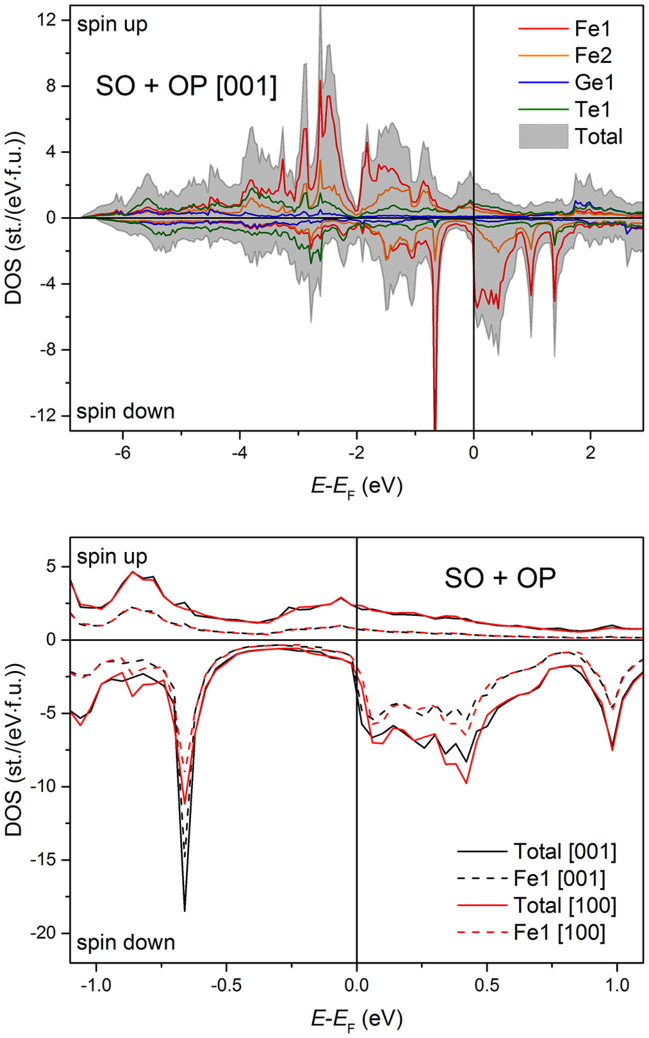

Figure 4. Top: calculated electronic density of states (DOS) for Fe_3GeTe_2 including spin−orbit coupling and orbital polarization (SO+OP). The [001] magnetization axis was used. The position of the Fermi level is indicated by the solid vertical line. Bottom: comparison between DOS plots for the [001] and [100] directions of magnetization axis. Fe1 contribution to the total DOS is shown as a dashed line.

Table 4. Calculated Magnetic Moments (μ_B) for the [001] and [100] Directions of Magnetization. The Spin (σ) and Orbital (l) Moments Result from Including Spin−Orbit Coupling only (SO) or Spin−Orbit Coupling and Orbital Polarization (SO+OP) within the Self-Consistent Calculations

	LSDA	SO		SO+OP	
[001]	σ	σ	l	σ	l
Fe1	2.47	2.46	0.10	2.46	0.16
Fe2	1.51	1.51	0.03	1.51	0.06
Ge1	−0.22	−0.22	0.01	−0.22	0.01
Te1	−0.01	−0.01	−0.04	−0.01	−0.04
total	12.4	12.4	0.32	12.4	0.62

	SO		SO+OP	
[100]	σ	l	σ	l
Fe1	2.46	0.10	2.46	0.20
Fe2	1.52	0.06	1.52	0.11
Ge1	−0.22	0.01	−0.22	0.01
Te1	−0.01	−0.01	−0.01	−0.01
total	12.4	0.5	12.4	1.0

the c direction.[18] In contrast, the field applied in the ab plane leads to a slower magnetization process, and at 5 T, the saturation is not reached yet.[18] In our case, the data are averaged over all field directions. The sizable magnetocrystalline anisotropy may then impede saturation for the in-plane orientation of the field. Indeed, the calculated anisotropy of about 4.2 meV/f.u. or 1.4 meV/Fe corresponds to a sizable magnetic field of 12 T assuming $g = 2$. However, the fact that we do not observe saturation even at 14 T might indicate a more complex nature of the magnetic ground state with, e.g., antiferromagnetic interactions between the Fe1 and Fe2 sublattices additionally impeding saturation in the applied field.

Neutron Diffraction. To shed light on the magnetic structure of $Fe_{2.9}GeTe_2$, we carried out neutron powder diffraction experiments at temperatures between 1.5 and 300 K (Tables 5 and 6). From the magnetic susceptibility measurements, the Curie temperature was found to be $T_C \sim 225$ K. However, the NPD pattern taken at $T = 1.5$ K has no additional magnetic peaks, which means that the magnetic structure is commensurate with the crystal structure, and $\vec{k} = 0$. Indeed, the refinement of the $T = 1.5$ K data converged to the ferromagnetic solution with the magnetic moments aligned along the c direction (Figure 6). The unavoidable overlap between the nuclear and magnetic reflections on the NPD patterns leads to strong correlations between individual refined parameters. To reduce these correlations, we fixed the M(Fe1)/M(Fe2) ratio to the value obtained at $T = 1.5$ K and studied the evolution of the magnetic structure for the entire temperature range. The resulting temperature dependence of magnetic moments is shown in the inset of Figure 6. The Fe1 and Fe2 magnetic moments gradually decrease upon heating and become zero when $T > T_C$.

NPD study reveals that $Fe_{2.9}GeTe_2$ possesses a commensurate ferromagnetic structure at low temperatures, which excludes more complex types of magnetic ordering from the consideration. Therefore, the unusual $M(H)$ behavior, found for $Fe_{2.9}GeTe_2$ at low temperatures, is not connected to the type of ordering, and the saturation of magnetic moment is impeded mostly by the magnetocrystalline anisotropy of $Fe_{2.9}GeTe_2$.

The total magnetic moment obtained from the NPD data, 1.8 μ_B per Fe atom, is in reasonable agreement with $M_S = 1.6$ μ_B/Fe taken from the single-crystal magnetization data.[18] On the other hand, our LSDA-based band structure calculations presented above overestimate the total magnetic moment, because spin fluctuations are not accounted for by LDA. The obtained value of $T_C \sim 230$ K from the NPD data agrees well with that derived from the Fisher's heat capacity plot (Figure 5b) and with the values presented in the literature.[6,18]

Mössbauer Spectroscopy. The ^{57}Fe Mössbauer spectrum of $Fe_{2.9}GeTe_2$ at 300 K consists of an asymmetric paramagnetic doublet with broadened components (Figure 7a). This spectrum cannot be described as a superposition of only two quadrupole doublets corresponding to the iron atoms on the Fe1 and Fe2 sites. Additional components are required and may be caused by the presence of vacancies in the nearest Fe1 environment, which emerge from the partial occupation of the Fe2 site. Therefore, the experimental spectrum was analyzed as a superposition of a distribution function $p(\Delta)$ of the

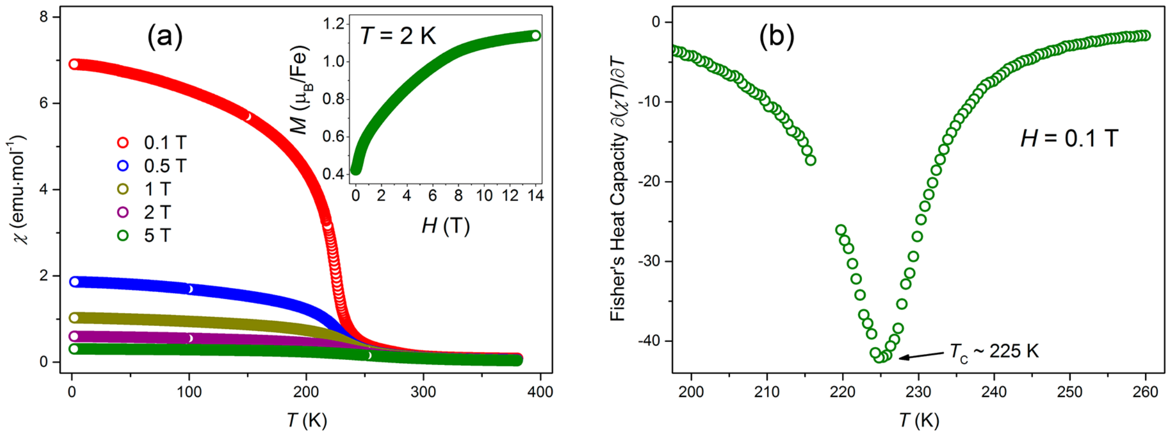

Figure 5. (a) Magnetic susceptibility χ versus T plot in different applied fields. The inset shows the magnetization curve taken at T = 2 K. (b) Plot of Fisher's heat capacity versus T.

Table 5. Crystal Data Collection and Refinement Parameters for $Fe_{2.9}GeTe_2$ at 300 and 1.5 K from NPD Data

parameter	300 K	1.5 K
space group	$P6_3/mmc$ (No. 194)	$P6_3/mm'c'$ (No. 194)
a [Å]	4.0045(3)	3.9912(3)
c [Å]	16.376(2)	16.296(2)
V [Å^3]	227.43(3)	224.81(4)
Z	2	2
ρ_{calc} [g·cm^{-3}]	7.15	7.23
2θ range [deg]	5−91	5−91
R_p (×10^{-2})	6.4	6.6
R_{wp} (×10^{-2})	8.5	8.7
GOF	4.5	4.9
M(Fe1) [μ_B]	0	1.95(5)
M(Fe2) [μ_B]	0	1.56(4)

Table 6. Atomic Parameters for $Fe_{2.9}GeTe_2$ at 300 and 1.5 K (*in Italics*) from NPD Data

atom	site	x	y	z	occupancy
Fe1	4e	0	0	0.6719(2)	1
		0	*0*	*0.6719(2)*	
Fe2	2c	2/3	1/3	3/4	0.9
		2/3	*1/3*	*3/4*	
Ge1	2d	1/3	2/3	3/4	1
		1/3	*2/3*	*3/4*	
Te1	4f	2/3	1/3	0.5901(5)	1
		2/3	*1/3*	*0.5895(4)*	

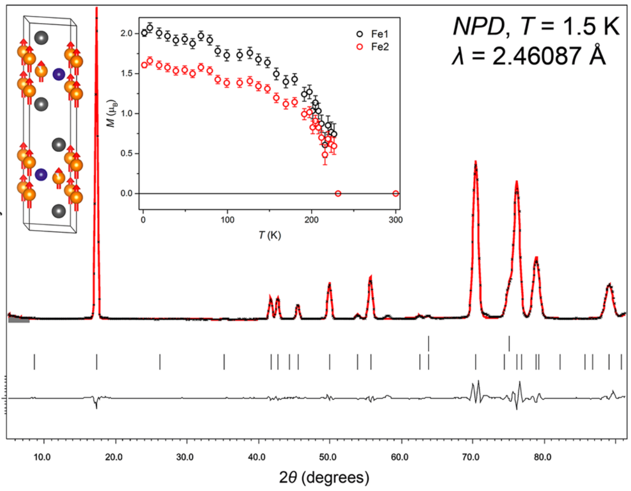

Figure 6. Experimental (black points) and calculated (red line) neutron powder diffraction patterns of $Fe_{2.9}GeTe_2$ taken at T = 1.5 K. Peak positions are given by black ticks: the top row belongs to the aluminum container, the bottom row: $Fe_{2.9}GeTe_2$. The difference plot is shown as a black line in the bottom part. The inset shows temperature dependence of the Fe1 and Fe2 magnetic moments. The corresponding magnetic structure is shown in the left part of the figure; Fe, gold; Ge, blue; Te, gray.

quadrupole splitting (Δ), corresponding to the iron atoms on the Fe1 site, and a unique quadrupole doublet for the Fe2 site (Figure 7a). In the distribution $p(\Delta)$, we assumed a linear correlation between the quadrupole splitting (Δ) and isomer shift (δ) values $\Delta_i = a + b\delta_i$, where a and b are fitting parameters.[16] The resulting $p(\Delta)$ (Figure 7b) has two main peaks, indicating that iron atoms on the Fe1 site have two nonequivalent environments, $(Fe1)_A$ and $(Fe1)_B$, with the average $\langle\Delta\rangle$ values of 0.33 and 0.51 mm/s, respectively. According to our model, the peak with the highest intensity in the $p(\Delta)$ distribution corresponds to the iron atoms on the Fe1 site with the "perfect" local environment (1Fe1, 3Fe2, 3Ge, 3Te). The second low intensity peak with the larger value of the quadrupole splitting can be related to the iron atoms on the Fe1 site having one Fe2 vacancy in the local environment (1Fe1, V_{Fe2}, 2Fe2, 3Ge, 3Te).

Taking into account the $p(\Delta)$ distribution analysis, we described the experimental spectrum as a superposition of three quadrupole doublets, $(Fe1)_A$, $(Fe1)_B$, and Fe2, with very close values of line width (W), but different isomer shifts (δ) and quadrupole splittings (Δ) (Figure 8). The resulting ratio of the partial contributions $I_A/I_B \approx 3.0$ for the two environments within the Fe1 site is in excellent agreement with the expected one from the binomial distribution (Table 7). This result indicates a random distribution of vacancies V_{Fe2} on the Fe2 site in the $Fe_{2.9}GeTe_2$ crystal structure. An unexpected result is that the removal of one Fe2 neighbor from the local environment of the Fe1 atom leads to the substantial reduction of the corresponding isomer shift value, $\delta_A - \delta_B \approx 0.11$ mm/s at 300 K (we observe negative correlation $b < 0$ in the $p(\Delta)$ distribution). On the contrary, the iron atoms on the Fe1 and Fe2 sites with different, but "perfect", local surroundings are characterized by the similar values of isomer shifts (Table 7).

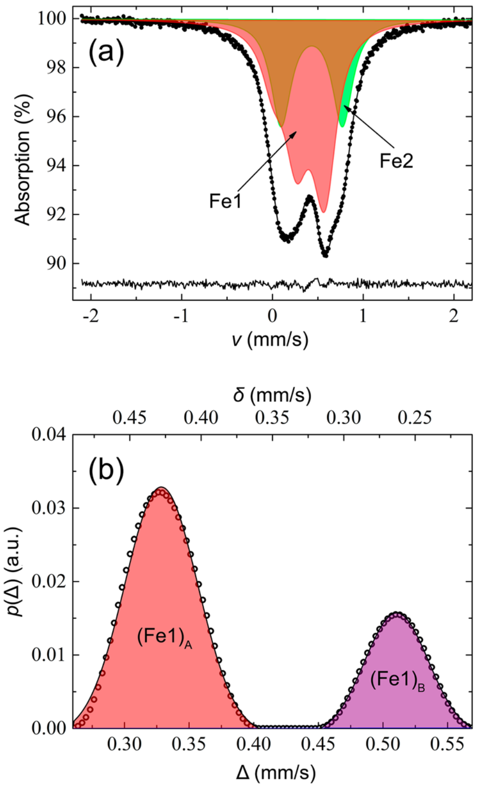

Figure 7. (a) ^{57}Fe Mössbauer spectrum of $Fe_{2.9}GeTe_2$ at 300 K. The solid red lines are a simulation of the experimental spectra as described in the text. (b) The distribution $p(\Delta)$ of quadrupole splitting $\Delta$for the Fe1 subspectrum resulting from the simulation.

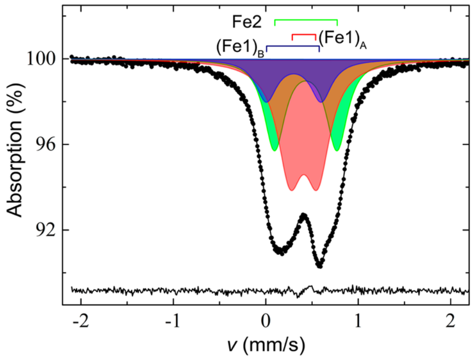

Figure 8. ^{57}Fe Mössbauer spectrum of $Fe_{2.9}GeTe_2$ at 300 K ($T \gg T_C$). The solid line is the result of fitting using a "discrete" model as described in the text.

The noticeable difference in the quadrupole splitting values $\Delta_A \ll \Delta_2$ indicates that the Fe1 and Fe2 sites in the $Fe_{2.9}GeTe_2$ crystal structure have a significantly different local environment. To confirm the assignment of the partial spectra to individual iron positions, we calculated the lattice contribution (V_{ij}) to the electric field gradient (EFG) tensor at the ^{57}Fe nuclei using the crystallographic parameters of $Fe_{2.9}GeTe_2$ (Tables 1 and 2). After diagonalization, the main EFG tensor components were used to estimate the quadrupole splitting values

$$\Delta^{\mathrm{theor}} = (1 - \gamma_\infty)eQV_{zz}(1 + 1/3\eta^2)^{1/2}$$

where γ_∞ is the Sternheimer's antishielding factor ($\gamma_\infty = -9.14$); eQ is the nucleus quadrupole moment (for ^{57}Fe, $eQ = 0.15$ barn[19]), $\eta = (V_{xx} - V_{yy})/V_{zz}$ is the parameter of asymmetry; and V_{ii} are the main components of the EFG tensor. The quadrupole splittings calculated by the above equation are presented in Table 7. The main factor that can be responsible for the observed discrepancy between the Δ^{calc} and Δ^{exp} values for the Fe2 site is the uncertainty in choosing the effective charges of the ions (Fe, Ge, Te) and the nucleus quadrupole moment eQ for the ^{57}Fe nuclei. However, our calculations correctly predict the ratio $\Delta_A^{\mathrm{calc}}/\Delta_2^{\mathrm{calc}} \approx 1.7$, which is in good agreement with the experimental value $\Delta_A^{\mathrm{exp}}/\Delta_2^{\mathrm{exp}} \approx 2.2$. Thus, we conclude that our model of randomly distributed Fe vacancies is fully adequate, and its subspectra $(Fe1)_{A,B}$ and Fe2 are correctly assigned to individual Fe sites in the $Fe_{2.9}GeTe_2$ crystal structure.

In the low-temperature regime, the ^{57}Fe Mössbauer spectra show a diffuse Zeeman resonance absorption (Figure 9a) that points to the existence of hyperfine magnetic fields (H_{hf}) at the ^{57}Fe nuclei. We determined the temperature $T \approx 225$ K, at which the magnetic hyperfine structure of the spectra completely disappears, which is very close to the temperature of phase transition, T_C. At low temperatures, the ^{57}Fe nuclei experience combined interactions of a hyperfine magnetic field (H_{hf}) and the electric field gradient (EFG). Due to the electric quadrupole interactions, if $H_{\mathrm{hf}} \gg eQV_{zz}$, the first-order quadrupole shift ε_Q is given by the equation[20]

$$\varepsilon_Q = 1/4eQV_{zz}(3/2\cos^2\theta + 1/2\eta\sin^2\theta\cos 2\varphi - 1/2)$$

where θ and φ are the polar coordinates of the H_{hf} direction in the (X, Y, Z) frame, which is defined by the main axes of the EFG tensor. The observed very complicated hyperfine magnetic structure may originate from the fact that the relative orientation of the magnetization direction (which evidently is the hyperfine field H_{hf} direction) with respect to the principal EFG axes denoted by the θ, φ angles in the equation is different for the crystallographically equivalent iron atoms in the crystal structure of $Fe_{2.9}GeTe_2$. Furthermore, the magnitude of the observed hyperfine fields associated with these iron atoms can be also different due to the existence of anisotropic hyperfine fields ΔH_{an}, whose origin is not well understood.[21]

On the basis of the above results for the paramagnetic spectra (Figure 7), which reveal three subspectra for the iron atoms, we reconstructed three hyperfine field distributions $p_i(H_{\mathrm{hf}})$ (Figure 9b), assuming that the quadrupole shift (ε_Q) is linear with the value of H_{hf}.[16] The analysis of these distributions gives the average values of quadrupole shifts $\langle\varepsilon_{Qi}\rangle$ and hyperfine fields $\langle H_{\mathrm{hf}}(i)\rangle$ (Table 8). The first $p_1(H_{\mathrm{hf}})$ distribution with the highest value of the hyperfine field $\langle H_{\mathrm{hf}}(1)\rangle$ and the partial contribution $I_1 \approx 50\%$ to the experimental spectrum (Table 8) can be definitively attributed to the iron atoms on the $(Fe1)_A$

Table 7. Hyperfine Parameters of the ^{57}Fe Mössbauer Spectrum of $Fe_{2.9}GeTe_2$ at 300 K

site	δ [mm/s]	Δ [mm/s]	Δ^{calc} [mm/s]	W [mm/s]	I^{exp} [%]	I^{calc} [%]
$(Fe1)_A$	0.41(1)	0.30(1)	0.31	0.33(1)	50.0(10)	51.72
$(Fe1)_B$	0.30(1)	0.59(1)		0.28(2)	16.7(12)	17.24
Fe2	0.43(1)	0.68(1)	0.53	0.27(1)	33.3(22)	31.04

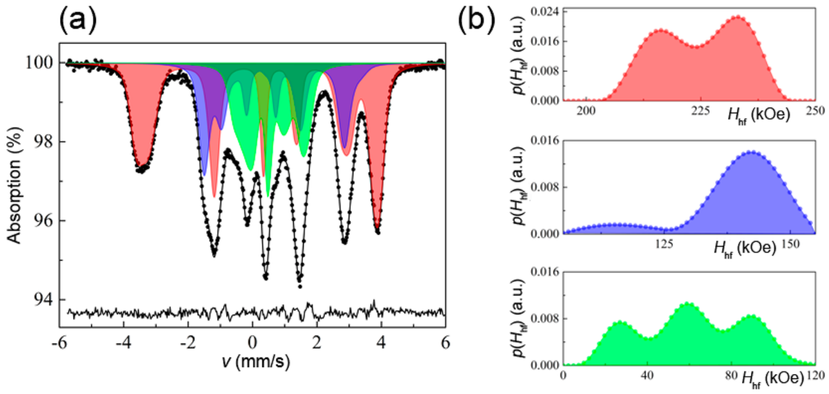

Figure 9. (a) ^{57}Fe Mössbauer spectrum of $Fe_{2.9}GeTe_2$ at 77 K. The solid red lines are a simulation of the experimental spectra as described in the text. (b) The hyperfine field distributions $p(H_{hf})$ resulting from simulation of the spectra.

Table 8. Hyperfine Parameters of the ^{57}Fe Mössbauer Spectrum of $Fe_{2.9}GeTe_2$ at 77 K

site	$\langle\delta\rangle$ [mm/s]	$\langle\varepsilon\rangle$ [mm/s]	$\langle H_{hf}\rangle$ [kOe]	I^{exp} [%]	I^{calc} [%]
$(Fe1)_A$	0.54(2)	−0.37(2)	226(2)	47.8(2)	51.72
$(Fe1)_B$	0.47(3)	0.20(3)	141(1)	25.1(2)	17.24
Fe2	0.55(2)	0.02(8)	56(2)	27.1(2)	31.04

site having a “perfect” environment. The bimodal profile of this distribution ($H_{max1} - H_{max2} \approx 20$ kOe) (Figure 9b) is related to the angular dependences of the quadrupole shift and anisotropic dipolar contribution ΔH_{dip}.[22] Therefore, in this structure, the iron atoms are placed on crystallographycally equivalent $(Fe1)_A$ sites, which are characterized by two different local principal EFG axes, giving rise to the complex spectrum in the magnetic state. Using the effective proportionality constant $A = 100 \div 115$ kOe/μ_B (hyperfine coupling constant), we estimated from $\langle H_{hf}(1)\rangle$ the magnetic moment per $(Fe1)_A$ atom $M(Fe1) = \langle H_{hf}(1)\rangle/A$. The obtained value of 2.11(14) μ_B agrees well with the results of NPD ($M(Fe1) = 2.07(2)$ μ_B). The unexpected result is the noticeable increase of the mean quadrupole shift value $\langle\varepsilon_{Q1}\rangle \approx 0.32$ mm/s at $T < T_C$ in comparison with the magnitude $\varepsilon_{Q1} = \Delta_A/2$ at $T = 300$ K (Table 7). This finding that cannot be explained by the conventional temperature dependence of the lattice contribution to the EFG on ^{57}Fe nuclei[20] might indicate an additional distortion due to a local magnetoelastic coupling at $T < T_C$.[23]

It is less obvious, how to determine the other two distributions $p_2(H_{hf})$ and $p_3(H_{hf})$ (Figure 9b) having nearly the same partial contributions $I_2 \approx I_3$, but very different mean hyperfine fields $\langle H_{hf}(2)\rangle$ and $\langle H_{hf}(3)\rangle$ (Table 8). Considering the $\langle H_{hf}(2)\rangle$ value, we estimated the magnetic moment $\langle H_{hf}(2)\rangle/A = 1.31(17)$ μ_B, which is close to the NPD results for $M(Fe2) = 1.66(2)$ μ_B. The discrepancy between the NPD and Mössbauer data may be attributed to the additional dipole contribution (H_{dip}) to the total hyperfine field H_{hf}, which is proportional to the EFG on ^{57}Fe nuclei $H_{dip} = (\mu_B/e)V_{zz}$.[22a] Taking into account that the quadrupole splitting $\Delta_2 \approx eQV_{zz}$ has the highest value at $T > T_C$ (Table 7), the dipole contribution H_{dip} should be most important for the Fe2 site in the $Fe_{2.9}GeTe_2$ crystal structure. Finally, the third $p_3(H_{hf})$ distribution can be attributed to the $(Fe1)_B$ atoms having one vacancy V_{Fe2} in the nearest surrounding. The three-modal profile of this distribution corresponds to different locations of V_{Fe2} around the $(Fe1)_B$ site. The low value of the mean hyperfine $\langle H_{hf}(3)\rangle$ field and the complex profile of the $p_3(H_{hf})$ distribution can be associated with the broken magnetic Fe1−Fe2 exchange interactions causing local magnetic frustration and relaxation phenomena.[24]

Magnetocaloric Effect and Thermoelectric Properties of $Fe_{2.9}GeTe_2$. Having investigated the local and bulk magnetic structure of $Fe_{2.9}GeTe_2$, we demonstrate how it manifests itself in functional properties of this material. First, we studied the magnetocaloric effect using the magnetization data at different temperatures. At $T = 220$ and 240 K, just below and above the

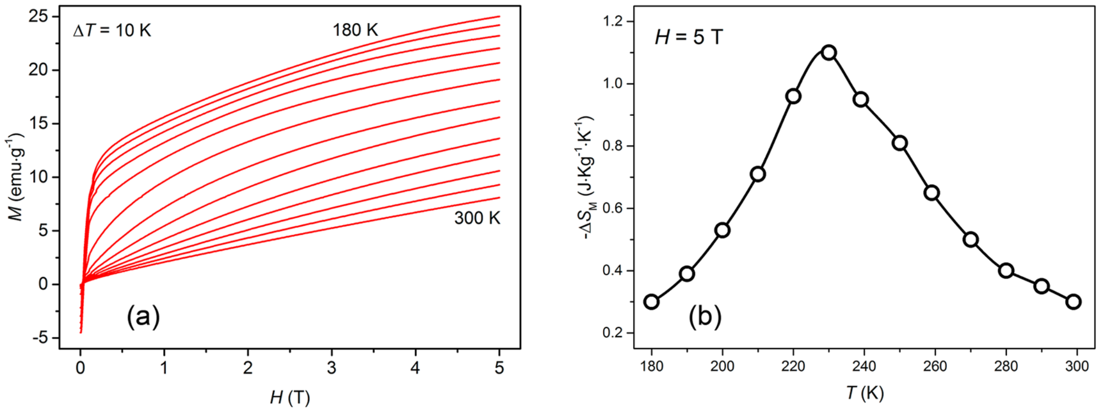

Figure 10. (a) Isothermal magnetization curves measured at temperatures between 180 and 300 K with a step of $\Delta T = 10$ K. (b) Plot of magnetic entropy change ($-\Delta S_M$) calculated from the $M(H)$ data.

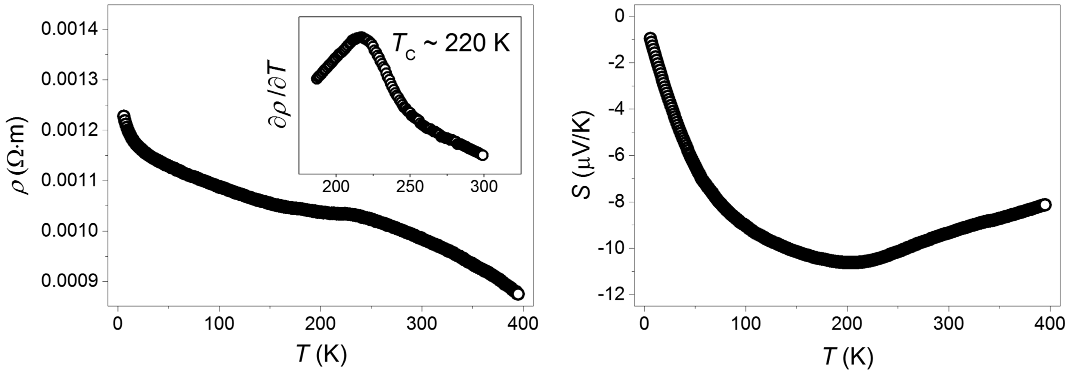

Figure 11. Temperature dependence of the resistivity and Seebeck coefficient for $Fe_{2.9}GeTe_2$ measured in zero magnetic field. The inset shows $\partial\rho/\partial T$ plot around the transition.

transition temperature, $M(H)$ curves are fully reversible while increasing and decreasing the magnetic field, indicating that the hysteretic losses are negligible and will not affect further calculations. It is known that the magnetic entropy change can be calculated from $M(H)$ curves using the following equation[25]

$$\Delta S = 1/\Delta T\left(\int_0^H M(T + \Delta T)dH - \int_0^H M(T)dH\right)$$

where ΔT means the increment of measurement temperature. Experimental $M(H)$ curves from 300 to 180 K with the increment of $\Delta T = 10$ K (Figure 10a) were used in calculations, resulting in negative values of ΔS (Figure 10b). The $-\Delta S$ value at 5 T is less than 1.2 J·kg^{-1}·K^{-1}. This value is much lower than those for large and giant MCE materials at their magnetic transition temperatures ($-\Delta S > 15$ J·kg^{-1}·K^{-1}, for instance[25−27]). The low value of $-\Delta S$ for $Fe_{2.9}GeTe_2$ is rooted in the reversibility of the $M(H)$ curves and in the absence of any structural changes at $T = T_C$, as shown by our NPD experiments.

Second, we studied transport and thermoelectric properties of $Fe_{2.9}GeTe_2$. Resistivity decreases with increasing temperature (Figure 11), but the temperature dependence of ρ does not follow the activation behavior. Additionally, the absolute values of the Seebeck coefficient do not exceed 12 μV/K, which is typical for metallic conductors. Thus, $Fe_{2.9}GeTe_2$ could be regarded as a bad metal with the electrons being major carriers, since the Seebeck coefficient is negative in the whole investigated temperature range. The temperature dependence of the Seebeck coefficient reveals a minimum located around the transition temperature, T_C. This anomaly related to the ferromagnetic transition is also clearly seen on the $\partial\rho/\partial T$ plot presented in the inset of Figure 11, corroborating the magnetic susceptibility measurements. Additionally, we found that the thermal conductivity of $Fe_{2.9}GeTe_2$ is below 1.5 W·m^{-1}·K^{-1} in the examined temperature range.

Magnetic and transport properties confirm the results of the electronic and magnetic structure calculations that revealed the metallic ferromagnetic ground state of Fe_3GeTe_2. These findings were further corroborated by heat capacity measurements presented in Figure 12. The data obtained in zero magnetic field could be satisfactory fitted with the equation $c_P = \gamma T + AT^3 + BT^{3/2}$, where γT is the electronic, AT^3 the lattice, and $BT^{3/2}$ the magnetic contributions to the total heat capacity of the specimen (the $BT^{3/2}$ term is used for ferromagnetically ordered compounds). To reduce possible correlations between individual parameters, we used the calculated value of $\gamma_{bare} = 9.2$ mJ·mol^{-1}·K^{-2}. The fit converged to $A = 0.773(7)$ mJ·mol^{-1}·K^{-4}, yielding the Debye temperature of $\Theta_D = 246$ K, and $B = 50.4(4)$ mJ·mol^{-1}·K$^{-5/2}$ showing that both electronic and magnetic contributions are significant, in good agreement with the proposed metallic and ferromagnetic ground state of Fe_3GeTe_2.

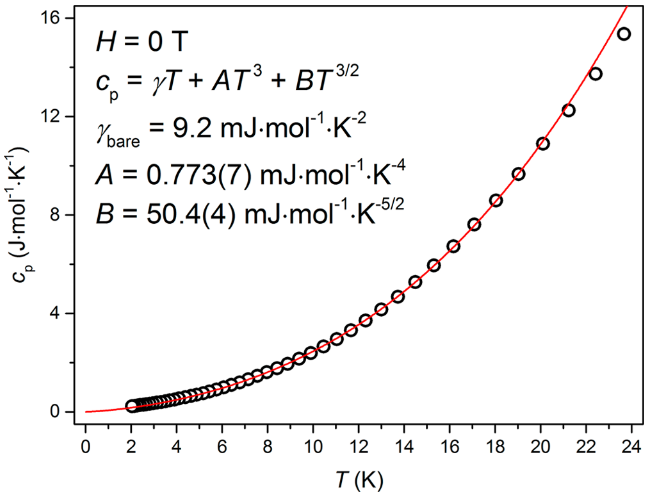

Figure 12. Heat capacity of $Fe_{2.9}GeTe_2$ in zero magnetic field at low temperature. Experimental data are shown as black open circles; fitting curve is presented as a red line.

■ CONCLUDING REMARKS

Fe-based telluride $Fe_{3-\delta}GeTe_2$ is formed for $0 < \delta < 0.3$ and features a layered crystal structure comprising weakly coupled $[Fe_3GeTe_2]$ slabs. Band-structure calculations put forward a metallic and ferromagnetic ground state with largely itinerant magnetic moments pointing along the c direction in the hexagonal crystal structure. The ferromagnetic transition is clearly seen near 230 K from temperature dependences of the magnetic susceptibility, electrical resistivity, and Seebeck coefficient. Additionally, the strong magnetocrystalline anisotropy (MCA) of about 4.2 meV/f.u. has been revealed by band-structure calculations. Neutron diffraction confirms the ferromagnetic ground state with the local moments of 1.95(5) and 1.56(4) μ_B at $T = 1.5$ K on the Fe1 and Fe2 sites, respectively. On the other hand, Mössbauer spectroscopy reveals peculiarities related to the formation of Fe vacancies. The Mössbauer spectrum at room temperature has three main components that represent not only the averaged surroundings of the Fe1 and Fe2 atoms but also the fine structure including the vacancies located on the Fe2 site. The Mössbauer spectra are also sensitive to vacancies at low temperatures, where three components with different hyperfine fields form a complex spectrum.

Ferromagnetic behavior of $Fe_{2.9}GeTe_2$ is reflected in the functional properties of this material. A moderate magnetocaloric effect with the entropy change of 1.1 $J \cdot kg^{-1} \cdot K^{-1}$ at the external field of 5 T has been observed. However, the entropy change is much lower than in large and giant MCE materials.

■ ASSOCIATED CONTENT

Ⓢ Supporting Information

The Supporting Information is available free of charge on the ACS Publications website at DOI: 10.1021/acs.inorgchem.5b01260.

Neutron crystallographic file for $Fe_{2.9}GeTe_2$ at 1.5 K (CIF)

Neutron crystallographic files for $Fe_{2.9}GeTe_2$ at 300 K (CIF)

X-ray crystallographic files for $Fe_{2.9}GeTe_2$ at 300 K (CIF)

■ AUTHOR INFORMATION

Corresponding Author

*E-mail: shev@inorg.chem.msu.ru.

Notes

The authors declare no competing financial interest.

■ ACKNOWLEDGMENTS

The authors thank Dr. Sergey Kazakov for the help with XRD experiments. The work in Moscow has been supported by the Russian Science Foundation, grant no.14-13-00089. The work in Tallinn has been supported by the Mobilitas program of the ESF, grant MTT77. A.A.T. is also grateful for the financial support by the Federal Ministry for Education and Research under the Sofja Kovalevskaya Award of the Alexander von Humboldt Foundation. We acknowledge the use of a Bruker D8 Advance X-ray diffractometer purchased under the Lomonosov MSU program of development. This work is partially based on the experiments performed at the Swiss spallation neutron source SINQ, Paul Scherrer Institute (PSI), Villigen, Switzerland.

■ REFERENCES

(1) Hume-Rothery, W.; Powell, H. M. *Z. Kristallogr.* **1935**, *91*, 23–47.

(2) Fredrickson, D. C.; Lee, S.; Hoffmann, R. *Inorg. Chem.* **2004**, *43*, 6159–6167.

(3) Yannello, V. J.; Fredrickson, D. C. *Inorg. Chem.* **2014**, *53*, 10627–10631.

(4) (a) Graf, T.; Felser, C.; Parkin, S. S. P. *Prog. Solid State Chem.* **2011**, *39*, 1–50. (b) Häussermann, U.; Viklund, P.; Boström, M.; Norrestam, R.; Simak, S. I. *Phys. Rev. B: Condens. Matter Mater. Phys.* **2001**, *63*, 125118. (c) Gippius, A. A.; Verchenko, V.Yu.; Tkachev, A. V.; Gervits, N. E.; Lue, C. S.; Tsirlin, A. A.; Büttgen, N.; Krätschmer, W.; Baenitz, M.; Shatruk, M.; Shevelkov, A. V. *Phys. Rev. B: Condens. Matter Mater. Phys.* **2014**, *89*, 104426.

(5) Isaeva, A. A.; Makarevich, O. N.; Kuznetsov, A. N.; Doert, T.; Abakumov, A. M.; Van Tendeloo, G. *Eur. J. Inorg. Chem.* **2010**, *2010*, 1395–1404.

(6) Deiseroth, H. J.; Aleksandrov, K.; Reiner, C.; Kienle, L.; Kremer, R. K. *Eur. J. Inorg. Chem.* **2006**, *2006*, 1561–1567.

(7) Larsson, A. K.; Noren, L.; Withers, R. L.; Rundlöf, H. *J. Solid State Chem.* **2007**, *180*, 2723–2733.

(8) Litvinenko, O. N.; Kuznetsov, A. N.; Olenev, A. V.; Popovkin, B. A. *Russ. Chem. Bull.* **2007**, *56*, 1945–1947.

(9) Reynolds, T. K.; Kelley, R. F.; DiSalvo, F. J. *J. Alloys Compd.* **2004**, *366*, 136–144.

(10) Baranov, A. I.; Kloo, L.; Olenev, A. V.; Popovkin, B. A.; Romanenko, A. I.; Shevelkov, A. V. *J. Am. Chem. Soc.* **2001**, *123*, 12375–12379.

(11) Palatinus, L.; Chapuis, G. *J. Appl. Crystallogr.* **2007**, *40*, 786–790.

(12) Koepernik, K.; Eschrig, H. *Phys. Rev. B: Condens. Matter Mater. Phys.* **1999**, *59*, 1743.

(13) Perdew, J. P.; Wang, Y. *Phys. Rev. B: Condens. Matter Mater. Phys.* **1992**, *45*, 13244.

(14) Blöchl, P. E.; Jepsen, O.; Andersen, O. K. *Phys. Rev. B: Condens. Matter Mater. Phys.* **1994**, *49*, 16223.

(15) Nordström, L.; Brooks, M. S. S.; Johansson, B. *J. Phys.: Condens. Matter* **1992**, *4*, 3261.

(16) Matsnev, M. E.; Rusakov, V. S. *AIP Conf. Proc.* **2012**, *1489*, 178–185.

(17) (a) Ohoyama, T.; Kanematsu, K.; Yasukochi, K. *J. Phys. Soc. Jpn.* **1963**, *18*, 589. (b) Havinga, E. E.; Damsma, H.; Hokkeling, P. *J. Less-Common Met.* **1972**, *27*, 169–186.

(18) Chen, B.; Yang, J.; Wang, H.; Imai, M.; Ohta, H.; Michioka, Ch.; Yoshimura, K.; Fang, M. *J. Phys. Soc. Jpn.* **2013**, *82*, 124711.

(19) Keller, H.; Savic, I. M. *Phys. Rev. B: Condens. Matter Mater. Phys.* **1983**, *28*, 2638.

(20) Gütlich, P.; Bill, E.; Trautwein, A. X. *Mössbauer Spectroscopy and Transition Metal Chemistry*; Springer-Verlag: Berlin, 2011.

(21) Kulshreshtha, S. K.; Raj, P. *J. Phys. F: Met. Phys.* **1982**, *12*, 377–388.

(22) (a) Drijver, J. W.; Sinnema, S. G.; Woude, F. *J. Phys. F: Met. Phys.* **1976**, *6*, 2165–2177. (b) Kulshreshtha, S. K.; Raj, P. *J. Phys. F: Met. Phys.* **1981**, *11*, 281.

(23) Raj, P.; Kulshreshtha, S. K. *J. Phys. (Paris)* **1981**, *41*, 1487–1494.

(24) Gibb, T. C. *J. Mater. Chem.* **2001**, *11*, 456.

(25) Provenzano, V.; Shapiro, A. J.; Shull, R. D. *Nature* **2004**, *429*, 853.

(26) Singh, N. K.; Suresh, K. G.; Nigam, A. K.; Malik, S. K. *J. Appl. Phys.* **2005**, *97*, 10A301.

(27) Tan, X.; Chai, P.; Thompson, C. M.; Shatruk, M. *J. Am. Chem. Soc.* **2013**, *135*, 9553–9557.